International Journal of Nanomedicine

Dovepress
open access to scientific and medical research

Open Access Full Text Article

ORIGINAL RESEARCH

Development of Small HN Linked Radionuclide Iodine-125 for Nanocarrier Image Tracing in Mouse Model

Ronglin Ma[1,2,*], Chunya Ji[1,*], Mengdan Shen[2], Shujuan Xu[2], Guojia Fan[3], Chengcheng Wu[1], Qiang Yu[2], Linliang Yin[1]

[1]Center for Medical Ultrasound, The Affiliated Suzhou Hospital of Nanjing Medical University, Suzhou Municipal Hospital, Gusu School, Nanjing Medical University, Suzhou, Jiangsu, 215002, People's Republic of China; [2]Department of Gastroenterology, The Affiliated Suzhou Hospital of Nanjing Medical University, Suzhou Municipal Hospital, Gusu School, Nanjing Medical University, Suzhou, Jiangsu, 215002, People's Republic of China; [3]Center for Cytotoxicity Testing, Sanitation & Environment Technology Institute, Soochow University, Suzhou, Jiangsu, 215006, People's Republic of China

*These authors contributed equally to this work

Correspondence: Qiang Yu, Department of Gastroenterology, The Affiliated Suzhou Hospital of Nanjing Medical University, Suzhou Municipal Hospital, Gusu School, Nanjing Medical University, Jiangsu, People's Republic of China, Tel +86 512 62362045, Email yuqiang0102sz@163.com; Linliang Yin, Center for Medical Ultrasound, The Affiliated Suzhou Hospital of Nanjing Medical University, Suzhou Municipal Hospital, Gusu School, Nanjing Medical University, Jiangsu, People's Republic of China, Tel +86 13382183478, Email yllsznthello@hotmail.com

Background: Radionuclides have important roles in clinical tumor radiotherapy as they are used to kill tumor cells or as imaging agents for drug tracing. The application of radionuclides has been developing as an increasing number of nanomaterials are used to deliver radionuclides to tumor areas to kill tumor cells. However, promoting the efficient combination of radionuclides and nanocarriers (NCs), enhancing radionuclide loading efficiency, and avoiding environmental pollution caused by radionuclide overuse are important challenges that hinder their further development.

Methods: In the present study, a new small molecule compound (3-[[(2S)-2-hydroxy-3-(4-hydroxyphenyl)-1-carbonyl] amino]-alanine, abbreviation: HN, molecular formula: $C_{12}H_{16}N_2O_5$) was synthesized as a linker between radionuclide iodine-125 (^{125}I) and NCs to enable a more efficient binding between NCs and radionuclides.

Results: In vitro evidence indicated that the linker was able to bind ^{125}I with higher efficiency (labeling efficiency >80%) than that of tyrosine, as well as various NCs, such as cellulose nanofibers, metal oxide NCs, and graphene oxide. Single-photon emission computed tomography/computed tomography imaging demonstrated the biological distribution of ^{125}I-labeled NCs in different organs/tissues after administration in mice.

Conclusion: These results showed an improvement in radionuclide labeling efficiency for nanocarriers and provided an approach for nanocarrier image tracing.

Keywords: nanocarriers, radionuclide labeling, radionuclide ^{125}i, SPECT/CT imaging

Introduction

Iodine-125 (^{125}I) is a low-power radionuclide that is widely used in biomedicine, due to its simple decay process, safe tissue penetration distance, less damage to surrounding healthy tissues, and long action time.[1,2] Its uses include cholangiocarcinoma treatment,[3] prostate cancer treatment,[4] non-small cell cancer treatment,[5] thyroid tumor tissue examination,[6] bone densitometry,[7] and isotope imaging in the clinic.[8–10] The main mechanism of action for the use of ^{125}I is to place it at the tumor site and kill tumor cells directly using gamma rays (0.03548 MeV) released from its decay process, thereby partially or completely eliminating the lesions and avoiding the recurrence or distant metastasis.[11] In addition, ^{125}I can also serve as an imaging probe for nanocarriers (NCs),[12,13] tyrosine, and proteins[14,15] in theragnostics and drug tracing. ^{125}I labeling on the surface of NCs or proteins is well suited for the study of its physiological roles and metabolism due to its short half-life of 60.14 days.[16–18]

Received: 27 October 2023
Accepted: 15 February 2024
Published: 23 February 2024

Thus far, near-infrared fluorescence imaging remains one of the most common imaging methodologies for in vivo visualization of NCs and protein carriers. However, it has several limitations, such as poor spatial resolution and tissue penetration.[19–21] By contrast, radionuclide imaging has high sensitivity, strong anti-interference ability, and no tissue-penetrating limitations, which can accurately reflect the distribution of radionuclide-labeled NCs or protein carriers in real time in two- or three-dimensional space in vivo.[22] For example, Kostiv et al studied biodegradation, biocompatibility, and multiplatform use of nonpolymeric surface-coated ^{125}I-labeled upconversion nanoparticles using in vivo SPECT/CT imaging.[23] Black et al investigated tumor targeting and imaging using gold nanoparticle probes with ^{125}I.[24] Farrag et al implemented a comparative study on ^{125}I radiolabeling and biodistribution of core-shell silver/polymeric nanoparticle-based theragnostics for tumor targeting.[25] The synthesis of radionuclide-labeled nanomedicine carriers or proteins that can specifically target tissues or organs can offer additional diagnosis and treatment methods for a variety of clinical diseases.

Even though the development of radionuclide radiolabeling provided a more effective avenue towards the application of NCs, polymeric micelles, and protein carriers,[26–28] it faced many difficult technological challenges. How to best simplify the labeling steps, improve the labeling efficiency, prevent the excessive usage of radionuclides, and avoid carrier property alteration after radionuclide labeling are all questions that need to be addressed.[29] Currently, there are four radiolabeling strategies: ligand connection, direct bombardment, direct synthesis, and post-synthesis.[30] Of these, the method of integrating or attaching radionuclides onto the surface of pre-prepared carriers or attachment during chemical synthesis is the best in terms of avoiding carrier property alteration. For instance, Chen et al generated a radiolabeling method to label graphene oxide nanoparticles with radionuclide ^{131}I via simple mixing. This method did not influence radioactive activity or alter physico-chemical attributes such as size, shape and surface functional groups.[31] However, there has been no intensive study on radionuclides labeling efficiency in nanomaterials in previous studies. The effective use of radionuclides may avoid environmental pollution caused by their overuse.

To explore the labeling efficiency of radionuclides in NCs and visualize the metabolic distribution of different NCs in vivo using radionuclides in the present study, a novel small molecule compound was designed and synthesized as a linker between radionuclides and NCs based on the post-synthesis method. It was designed to bind both NCs and radionuclides. Its labeling efficiency for radionuclides was then tested and optimized. To visualize the in vivo interaction between various NCs with different properties and the organism, eight representative NCs with different compositions, shapes, sizes, and surface charges were prepared and collected. After the synthesis and characterization of these NCs, their radionuclide labeling efficiency in the presence of HN was investigated. Finally, NC tissue distribution was visualized in mice using SPECT/CT imaging after administration based on NC radionuclide labeling.

Materials and Methods

Sodium pyrosulfite, Na^{127}I, pyridine, lanthanum hydroxide, N, N-carbonyldiimidazole (CDI), dimethylformamide (DMF), dimethyl sulfoxide (DMSO) trifluoroacetic acid (TFA), acetic anhydride (Ac_2O), (3-aminopropyl) triethoxysilane (APTES), and K_2CO_3 were purchased from Aladdin Bio-Chem Technology Co., Ltd (Shanghai, China). Ultrafiltration tube (10Kd), polyethylenimine (PEI), 3-(4-hydroxyphenyl) lactic acid, N(α)-Boc-D-2,3-diaminopropionic acid, N-(3-dimethylaminopropyl)-N′-ethylcarbodiimide hydrochloride of commercial grade (EDC), N-hydroxysuccinimide (NHS) and 1,3,4,6-tetrachloro-3A,6A-diphenylglycouril were purchased from Sigma-Aldrich (St. Louis, MO, USA). ^{125}I was purchased from Shanghai GMS Pharmaceutical Co. Ltd. Methanol (chromatography pure), dichloromethane (DCM, analytical pure) and anhydrous ethanol (analytical pure) were from Sinopharm Chemical Reagent Co., Ltd. (Shanghai, China).

The Synthesis of Small-Molecule Compound HN

1) Preparation procedure for compound 2

Ac_2O (83.8 mg, 0.822 mmol) was added to a solution of 3-(4-hydroxyphenyl) lactic acid (compound 1, 50 mg, 0.274 mmol) and pyridine (53.5 mg, 0.687 mmol) in DCM (2 mL) at 15°C. The mixture was stirred at 15°C for 16 h and then concentrated in vacuo to obtain acetylated compound 1 (compound 2), which was used in subsequent experiments.

2) Preparation procedure for compound 3

CDI (80.1 mg, 0.494 mmol) was added to a solution of compound 2 (90 mg crude) in anhydrous DMF (2 mL) at 15°C. N(α)-BOC-D-2,3-diaminopropionic acid (compound 3, 112.1 mg, 0.549 mmol) was added after stirring for 0.5 h. Then, the

mixture was stirred at 15°C for 16 h. The resulting reaction mixture was concentrated in vacuo to obtain the HN precursor (compound 4).

3) Preparation procedure for compound 5

NaOH (54.9 mg, 1.37 mmol) was added to a solution of compound 4 (290 mg crude) in anhydrous MeOH (5 mL) at 15°C. The mixture was stirred at 15°C for 16 h. Liquid chromatography tandem mass spectrometry (LC-MS/MS) showed that compound 4 was consumed and that the mass value of compound 5 was detected. The resulting mixture was neutralized to a pH of 5 with HCl (1 M). Then, the solvent was removed to reduce pressure. The resulting residue was dissolved in MeOH (2 mL) and deionized water (DI H_2O, 2.0 mL) and purified with reversed-phase chromatography on a silica gel (water (0.05% HCl): CH_3CN: 30% to 70%) to obtain deacetylated HN (compound 5, 28.0 mg, 0.076 mmol, 27.7% yield over three steps) as a white solid.

4) Preparation procedure for compound 6

A solution of compound 5 (28.0 mg, 0.076 mmol) in anhydrous DCM (2 mL) and TFA (2 mL) was stirred at 15°C for 16 h. LC-MS/MS showed that compound 5 was consumed and that the mass value of compound 6 was detected. The resulting mixture was concentrated in vacuo to obtain the crude product. The resulting light-yellow oil was then dissolved in water (2 mL) and dried using lyophilization to generate a new small molecule HN (compound 6, 26.1 mg, TFA salt, 0.072 mmol, 94.1 yield) as a white solid.

Characterization of Compound HN

1) ^{1}H NMR analysis of HN

The structure of HN was determined using ^{1}H nuclear magnetic resonance (^{1}H NMR, Mettler Toledo, Switzerland). Briefly, 20 μL of HN (50 mg/mL) was dissolved in 0.5 mL of deuterium DMSO and placed into a nuclear magnetic tube with a diameter of 5 mm. The hydrogen spectrum data for HN were collected using ^{1}H NMR with the following parameters: each sample was scanned 64 times, the acquisition time was 2.9089 s, the working frequency was 400.05 MHz, and the spectral width was 8221.82 Hz.

2) LC-MS/MS analysis of HN

LC-MS/MS was carried out on an Agilent 1100 LC system (Santa Clara, CA, USA) coupled to an LTQ mass spectrometer (Thermo, MA, USA). Samples were separated in an Agilent ZORBAX RX-C18 column (4.6 mm × 250 mm, 5 μm, 100 Å) at a flow rate of 0.4 mL/min with an 80% mobile phase B in 20 min. Mobile phase A was 0.1% acetic acid solution in water. The injection sample volume was 5 μL, and the column was kept at 25°C. The LC eluent was directed to the MS for a full scan (50–1000 m/z) in positive ionization mode. The MS parameters were set as follows: capillary temperature of 325°C, source current of 4 μA, source voltage of 3.5 kV, aux gas flow rate of 6 arbitrary units (arb), sheath gas flow rate of 25 arb, and isolation width of 1.5 m/z. The MS data were analyzed using Xcalibur 3.0 software (Thermo, USA).

Synthesis and Characterization Analysis of Iodine-127 and Iodine-125 Labeled HN

1) Iodine-127 Labeled HN

Iodine-127 labeled HN (^{127}I-HN) was synthesized using a standard activator oxidation method.[17] Briefly, 0.3 mL of 1,3,4,6-tetrachloro-3A,6A-diphenylglycouril (5 mg/mL, 10 mg in 2 mL of trichloromethane) was dried under nitrogen and distributed throughout the inner wall of a 10-mL round bottom flask. Then, we added 0.33 μM $Na^{127}I$ and different concentrations of HN dissolved in 500 μL of KOH-H_3PO_4 solution with a pH of 7.0. The mixture was stirred gently for 30 min at 37°C. After a 30-min reaction, 2 μL of sodium metabisulfite solution (100 mg/mL) was added to terminate the reaction, and the mixture was placed into the solid phase extraction column activated by methanol and DI water. Then, the column was washed with 3 mL of deionized water and eluted with 5 mL of 80% methanol, which was evaporated until reaching a final volume of 100 μL.

2) LC-MS/MS and ICP-OES Analysis of Iodine-127 Labeled HN

LC-MS/MS was performed to detect the ^{127}I-HN as described in the above LC-MS/MS analysis of HN. Labeling efficiency of ^{127}I-HN was calculated using the following equation:

$$\text{Labeling efficiency}\ (\%) = \frac{A_a - A_b}{A_a} \times 100\%,$$

where A_a and A_b represent the peak HN area and the remaining HN detected using LC-MS/MS, respectively.

^{127}I-HN was also quantified using inductively coupled plasma optical emission spectra (ICP-OES, iCAP 7200 SERIES, Thermo, USA). Next, 0.1 mL of 5 mg/mL ^{127}I-HN was fully digested in 0.5 mL of HNO_3 and 1.0 mL of H_2O_2 in a sealed container. Then, 50 μL of dissolved ^{127}I-HN solution was diluted with 10 mL of DI H_2O. The diluted solutions were used to test the iodine content with ICP-OES. The iodine concentration was experimentally determined by referring to the iodine standard curve made using the Na^{127}I solution. Labeling efficiency of ^{127}I-HN was calculated using the following equation:

$$\text{Labeling efficiency}\ (\%) = \frac{A_c}{A_d} \times 100\%,$$

where A_c and A_d represent the concentrations of iodine in substrates Na^{127}I and ^{127}I-HN, respectively.

3) Synthesis and Analysis of Iodine-125 Labeled HN

Iodine-125 labeled HN (^{125}I-HN) was synthesized using a similar method as described for ^{127}I-HN with two minor changes. First, 0.33 μM Na^{127}I was replaced with 1.28 megacurie (mCi) Na^{125}I. Second, radiolabeling experiments were performed in the approved Radiological Laboratory of the State Key Laboratory of Radiation Medicine and Protection of Soochow University. In addition, the analysis of ^{125}I-HN was different from that of ^{127}I-HN. The labeling efficiency for ^{125}I-HN was directly calculated using a gamma counter (Packard, CobraII Auto gamma).

Preparation, Collection, and Characterization of Nanocarriers

Nanofibers, including CNF-1 and CNF-2, were prepared using the ultrasound-assisted TEMPO oxidation method. Uniform fiber suspension pulp at a concentration of about 1% was prepared with commercial softwood pulp (Catalyst Paper Corporation, Canada) before the oxidation treatment. TEMPO (16 mg), NaBr (100 mg), and various amounts of NaClO (150 mg, 375 mg, and 600 mg) were added into three sets of 1% softwood pulp (1 g) samples and their pH adjusted to 10. After oxidation at 25°C for 60 min, the resulting fibers were washed with ultra-pure water until achieving neutrality and homogenized at 80 MPa five times with a high-pressure homogenizer (AH08-100, ATS Engineering Inc., Canada) to obtain nanofibers of different lengths. PEI-functionalized CNF-1 (PEI-CNF-1) was prepared using PEI modification of negative CNF-1 utilizing EDC/NHS chemistry. First, EDC/NHS (100 mg/50 mg) and 10 mL of 5 mg/mL CNF were incubated with shaking for 2 h at 25°C. The precipitates were obtained by centrifugation (12,000 rpm, 30 min) and were further washed three times with DI H_2O. Afterward, the precipitates were suspended with 1 mL of 10 mg/mL PEI aqueous solution and stirred for 48 h to obtain PEI-CNFs. Finally, PEI-CNFs were collected using centrifugation (12,000 rpm, 30 min) and resuspended with 1.0 mL of DI H_2O.

CNTs purchased from Cheap Tubes Inc. (Brattleboro, USA) were used to synthesize COOH-CNTs according to a previous report.[32] To synthesize COOH-CNTs, pristine CNTs (1 g) were dispersed in 120 mL of concentrated H_2SO_4 and HNO_3 (3:1, v/v) solution and reacted for 30 min at 120°C. After cooling, the solutions were diluted 10-fold with DI H_2O, filtered through a 0.45-μm membrane, and washed to collect COOH-CNTs.

La_2O_3 was prepared based on a previously reported method with a few modifications.[32] Specifically, 0.217 g of $La(NO_3)_3 \cdot 6H_2O$ and 0.192 g of citric acid were dissolved in 20 mL of DI H_2O to react with 20 mL of 10% KOH under vigorous stirring. The mixture was reacted at 180°C for 15 h under magnetic stirring to form $La(OH)_3$, which was collected by centrifugation (5000 rpm, 30 min) and washed three times with DI H_2O. La_2O_3 nanoparticles were obtained using a 400°C calcination treatment for 4 h.

CeO_2, GO, and mesoporous SiO_2 were obtained from Nanostructured & Amorphous Materials (Houston, TX, USA).

The NC morphologies were observed using transmission electron microscopy (TEM; Tecnai G20, FEI, USA) at a voltage of 120 kV and atomic force microscopy (AFM, Nanoscope Icon, Veeco, USA). Drops of NCDI H_2O solution (50 μg/mL) were placed on a grid and mica plate and dried at room temperature for TEM and AFM observations, respectively. ENM zeta potentials and particle sizes in water were measured using dynamic light scattering (Zetasizer Nano ZS90, Malvern, UK).

Synthesis and Stability of Iodine-125 Labeled Nanocarriers

In order to visualize the distribution of NCs in animals, all NCs were labeled with ^{125}I (^{125}I-NCs). NC ^{125}I labeling experiments were divided into two steps: i) introduce the hydroxyl, carboxyl, or amino groups onto the surface of NCs; ii) covalently bind NCs to ^{125}I-HN using EDC/NHS covalent chemistry and investigate ^{125}I-NC stability.

1) NC Surface Modification

The NCs (CeO_2, La_2O_3, SiO_2) without the hydroxyl, carboxyl, or amino groups on their surface were first functionalized with APTES by dispersing the NCs in ethanol that contained 5% APTES and heating at 60°C for 3 h.

2) Investigation of ^{125}I-NC Synthesis and Stability

^{125}I-NCs were prepared using a diimide-activated amidation reaction.[33] Briefly, 5 mg of EDC and 10 mg of NHS were added into 200 μL of NCs (5.0 mg/mL) diluted with 800 μL of DI water. The mixture was stirred for 2 h at room temperature. The NC pellets were then collected by centrifugation (50,000 × *g*,10 min) to react with 1.06 mCi ^{125}I-HN for 2 h. Lastly, the ^{125}I-NCs were collected by centrifugation (1500 × *g*, 30 min) using Amicon filters (MWCO = 10 kDa) and washed several times with DI water until the radioactivity in the filtration solution was <15 μCi. Lastly, the ^{125}I-NCs were resuspended in 500 μL of DI water. For the stability assay of ^{125}I-NCs, 100 μCi I^{125}-NCs were added to 500 μL of phosphate-buffered saline, and the mixture was placed in a shaking water bath at 37°C for 14 days to observe whether ^{125}I was separated from the mixture. Labeling efficiency of ^{125}I-NCs was calculated using the following equation:

$$\text{Labeling efficiency}\,(\%) = \frac{A_e}{A_f} \times 100\%,$$

where A_e and A_f represent the radioactivity (mCi) of $Na^{125}I$ and ^{125}I-NCs, respectively.

SPECT/CT Imaging

Week-old female C57BL/6 mice were obtained from Gempharmatech Co., Ltd (Nanjing, China) and housed in SPF-class housing in a laboratory that was set up according to the SOOCHOW guidelines for care and treatment of laboratory animals. The protocols were approved by the Animal Research Committee at SOOCHOW. First, 300 μCi ^{125}I-NCs were delivered via intraperitoneal injection, intravenous injection, or intratracheal instillation into the C57BL/6 mice for SPECT/CT imaging (MILabs, Utrecht, the Netherlands) on days 1 and 5. The SPECT/CT image acquisition parameters were as follows: fast full scanning mode, SPECT/CT acquisition for 10 min followed by CT scanning for 2.17 min, and scanning at each angle for 30 min. Then, SPECT/CT imaging data were exported to u-SPECT and PMOD software for image reconstruction, display, and analysis.

Statistical Analysis

The values in all figures represent mean ± standard deviation. Statistical significance was determined using two-tailed Student's *t*–test for two-group analysis or one-way ANOVA for multiple group comparisons.

Results

Design, Synthesis, and Characterization of HN

To label NCs or compounds with ^{125}I, a novel small molecule compound was synthesized as a linker and named 3-[(2S)−2-hydroxy-3-(4-hydroxyphenyl)-1-carbonyl]amino]–alanine (abbreviation: HN, molecular weight: 268, chemical formula: $C_{12}H_{16}N_2O_5$). The HN design satisfied the following two functions: the ability to bind NCs and radionuclides. The binding principle of NCs to HN is that HN carboxylates (-COOH) can be reacted with primary amine ($-NH_2$) or hydroxyl (-OH) groups of NCs to form amide crosslinks using EDC/NHS chemistry.[32] The binding principle of radionuclides to HN is that hydrogen ions near phenolic hydroxyl group of HN were replaced with the radionuclide via the nucleophilic substitution reaction.[33] Thus, the linker HN consists of a phenolic hydroxyl group and a carboxylate group to bind to radionuclides and primary NC amines, respectively. Based on the above design, two reactants were used to synthesize linker HN. N(α)-Boc-D-2, 3-diaminopropionic acid enabled HN conjugation to NCs and 3-(4-hydroxyphenyl) lactic acid enabled HN labeling of radionuclides (Figure 1).

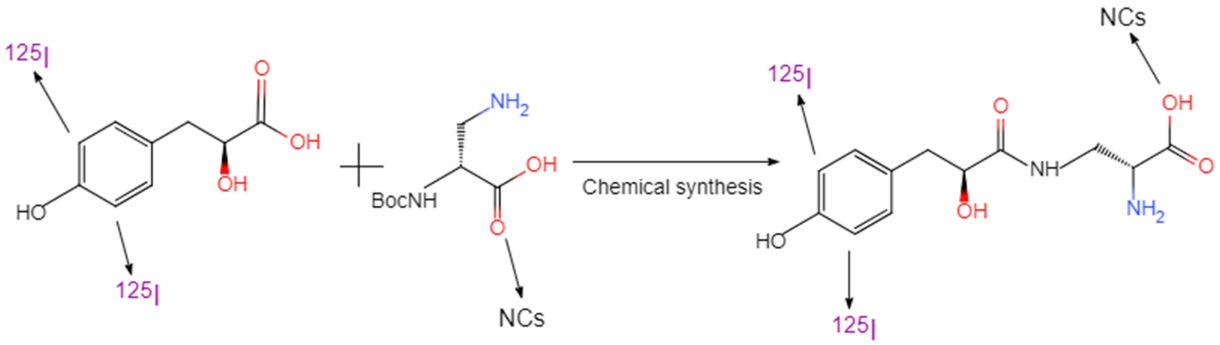

Figure 1 Schematic Diagram of HN Synthesis.

After confirming the two reactants, HN was synthesized in four steps shown in Figure 2. The first step was to protect the hydroxyl group in 3-(4-hydroxyphenyl) lactic acid (compound 1) to obtain compound 2 via acetylation. In the second step, compound 2 was reacted with N(α)-BOC-D-2,3-diaminopropionic acid (compound 3) to produce the HN precursor (compound 4). The third and fourth steps restored the hydroxyl and amino groups by deacetylation and Boc-deprotection of compound 4, ultimately forming the target product HN (compound 6). Finally, 2.0 mL of light-yellow oil was freeze-dried to calculate the HN yield, which reached 94.1%.

^{1}H NMR spectrum analysis was performed to determine the chemical structure of HN. ^{1}H NMR data (Figure 3A) were recorded in the following order: chemical shift (ppm), multiplicity (s, singlet; d, doublet; dd, double doublet; t, triplet; m, multiplet), coupling constant J (Hz), and integration. The data for compound HN were as follows: ^{1}H NMR (400 MHz, DMSO-d_6) δ: 9.18 (s, 1H), 8.09 (dt, J =15.6, 4 Hz, 2H), 7.37 (s, 1H), 7.00 (d, J = 5.2 Hz, 2H), 6.66 (d, J = 5.6 Hz, 2H), 5.61 (dd, J = 3.6, 15.2 Hz, 2H), 4.00 (t, J = 2.8 Hz, 1H), 3.91 (s, 1H), 2.90–2.86 (m, 2H), 2.62 (d, J = 1.2 Hz,1H), 2.39 (t, J = 0.8 Hz, 1H). The ^{1}H NMR data for HN showed signals for 16 hydrogen atoms, which was expected. To further confirm the composition and molecular weight of HN, the LC-MS/MS analysis results in Figure 3B showed a maximum peak at 2.2 min with molecular weight of 269 and 1.86 μM concentration in positive ion mode, which is consistent with its theoretical molecular weight. These results confirmed the structure of the synthetic compound HN.

Optimization of Parameters for HN Labeling

The feasibility of ^{125}I labeling was investigated after HN synthesis was completed. The chemical reaction equation for HN radionuclide labeling is shown in Figure 4A, indicating that two products were obtained as a result of these reactions according to the labeling number and location of non-radioactive ^{127}I. One product was HN with single non-radioactive ^{127}I and a molecular weight of 394, and the other product was HN with double non-radioactive ^{127}I with a molecular weight of 520.

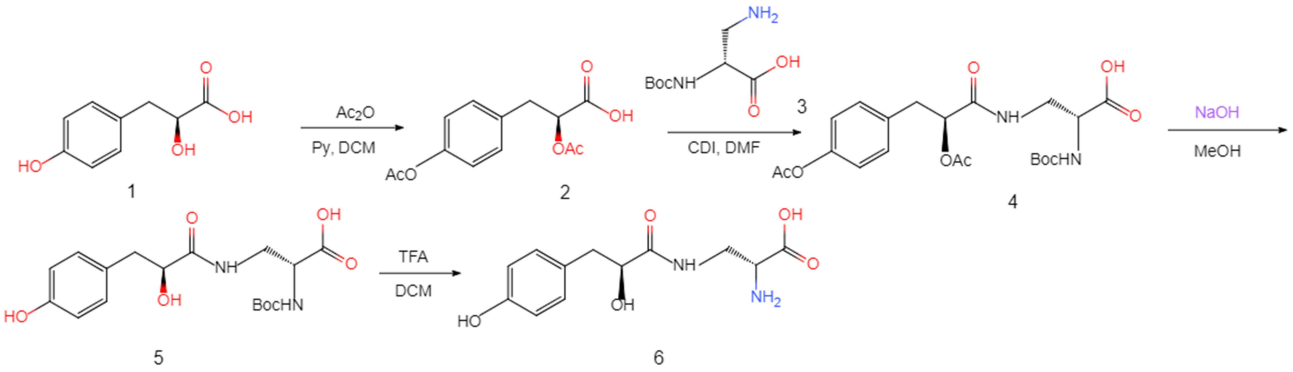

Figure 2 HN Synthesis HN synthesis procedure steps. i) Acetylation of compound 1 with Ac_2O in the presence of Py in DCM gave compound 2; ii) Reaction with compound 3 gave compound 4; iii) Deacetylation of compound 4 with NaOH gave compound 5 with 27.7% yield in MeOH; and iv) Boc-deprotection of compound 5 with TFA gave compound 6 with 94.1% yield in DCM.

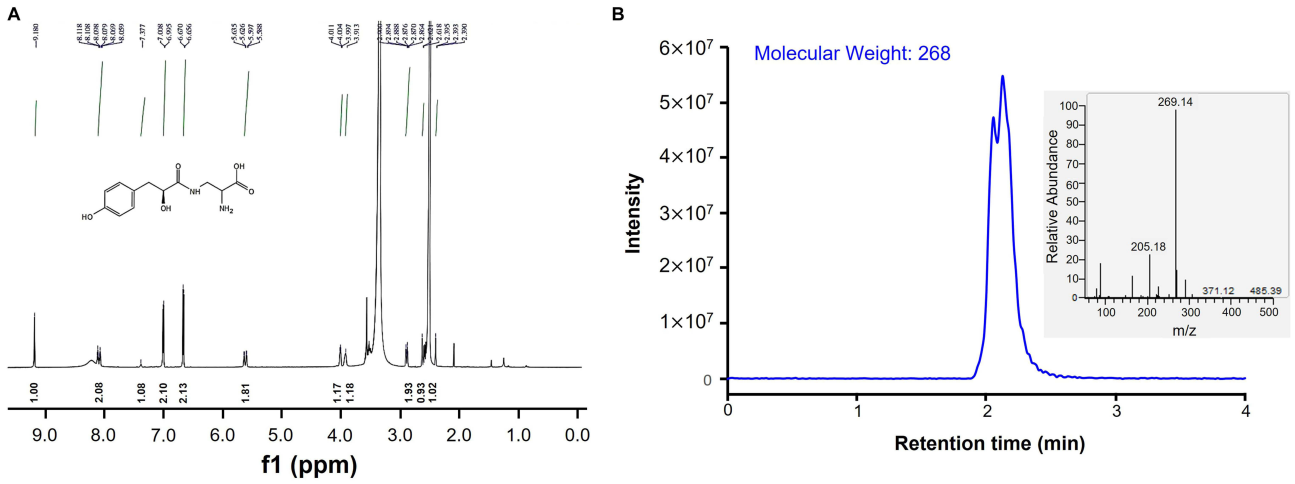

Figure 3 Structure Analysis of HN Using 1H NMR Spectrum and LC-MS/MS (**A**)^{1}H NMR analysis of HN; (**B**) LC-MS/MS analysis of HN. Reaction product HN was detected using LC-MS/MS in positive ion mode to obtain its molecular weight.

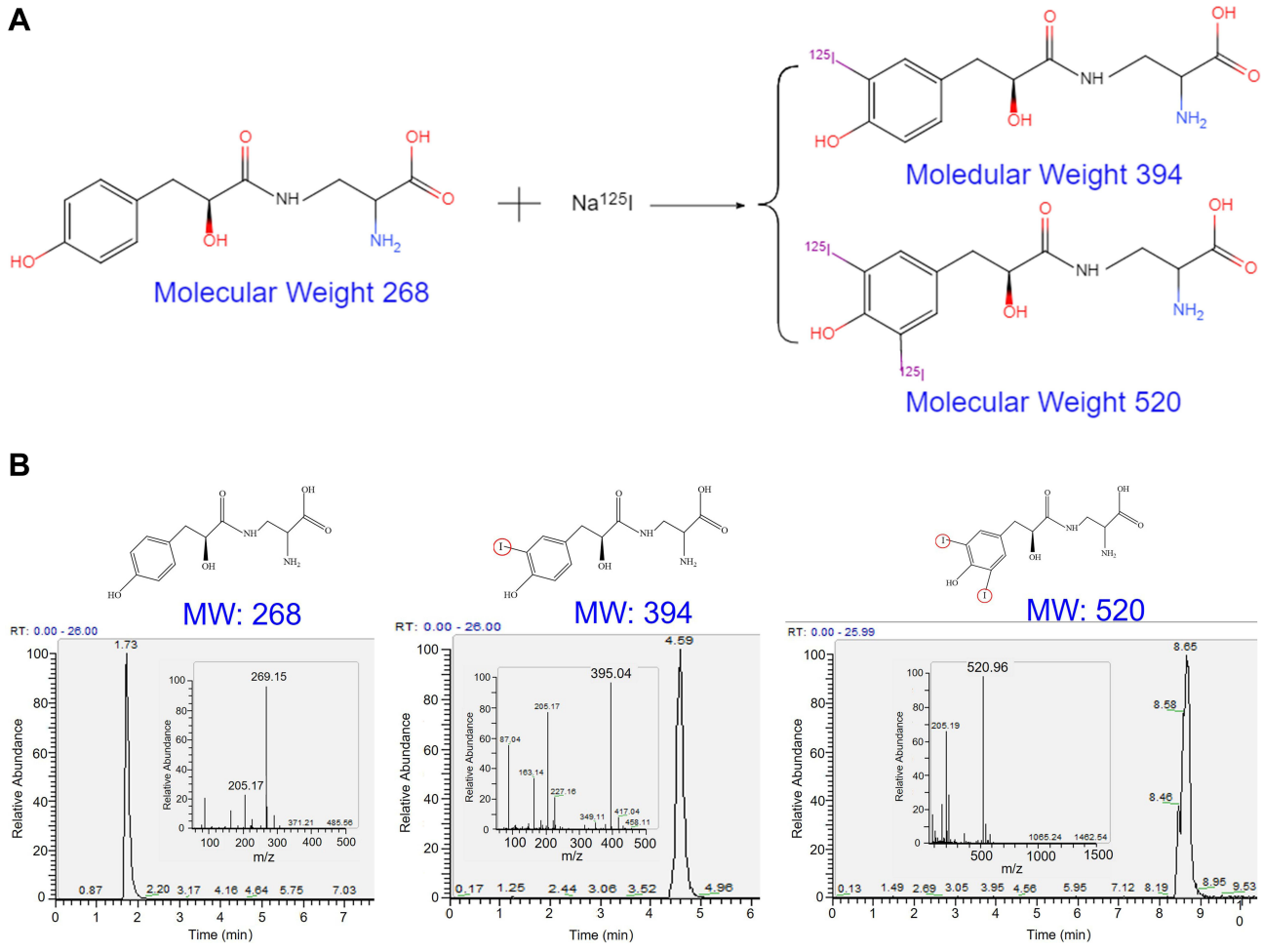

Figure 4 Schematic Illustration and Verification of Iodogen Labeling for HN (**A**) Schematic illustration of iodogen labeling for HN. When one hydrogen atom in the ortho-position of benzene hydroxyl group is replaced with iodogen, a single iodine-labeled HN is formed, and when two hydrogen atoms are substituted, double iodine-labeled HN is formed; (**B**) Verification of iodogen labeling for HN. Reaction products containing HN, single iodine-labeled HN, and double iodine-labeled HN were detected using LC-MS/MS in positive ion mode to obtain their molecular weight.

https://doi.org/10.2147/IJN.S446564 DovePress

In order to verify the above reaction mechanism, improve the labeling efficiency of ^{125}I, and avoid environmental pollution caused by unnecessary excessive use of radionuclides, the reaction parameters were optimized by replacing radioactive ^{125}I with non-radioactive ^{127}I. The HN-to-Na^{127}I ratio was set to 0.5:1, 1:1, 3:1, 5:1, and 10:1 (Table 1). The Na^{127}I concentration was fixed at 0.33 μM, while the HN concentration increased gradually. After the reaction, the reaction product was collected using a C_{18} column and processed using the LC-MS/MS method in positive ion mode to obtain the molecular weight and area of each peak. Three peaks with molecular weights of 269, 395, and 521 were observed in the reaction products with the ratio increase from 1:1 to 10:1 (Figures 4B–D and Table 1). In addition, the peak area with a molecular weight of 269 increased gradually with HN proportion increase, the peak area of 395 increased at first and then tended to remain stable, while the peak area of 521 increased at first and then decreased. By calculating the peak area, it was concluded that the labeling efficiency of ^{127}I-HN (calculated using the formula from section 2.4.2) was close to 100% when the HN-to- Na^{127}I ratio was 0.5:1. The labeling efficiency of ^{127}I-HN gradually decreased with the increase in the HN concentration. It was speculated that this was likely because Na^{127}I was in an excess concentration state at a ratio of 0.5:1 and all HNs were labeled with double ^{127}I. However, HN was in an excess concentration state as the ratio increased and the content of prime HN gradually increased. Thus, the labeling efficiency gradually decreased.

To further verify the labeling efficiency of ^{127}I-HN, the iodine content in ^{127}I-HN synthesized at two different HN-to-Na^{127}I ratios (0.5:1 and 5:1) was measured using ICP-OES, which was calculated using the formula described above (Table 2). The labeling efficiency of ^{127}I-HN was close to 100% when the HN-to-Na^{127}I ratio was 0.5:1. In addition, the labeling efficiency calculated based on the content change of iodine in Na^{127}I was not significantly improved when the ratio was 5:1, indicating that all of ^{127}I was accepted by the HN substrate. These results were consistent with those obtained by LC-MS/MS and further demonstrated that HN can be used as a linker for iodine labeling.

After the successful HN labeling with Na^{127}I, the optimized reaction conditions were used to complete the HN labeling with ^{125}I. Because ^{125}I was measured using radioactive activity and had a half-life, the actual molarity of Na^{125}I was unavailable. However, according to 1.28 mCi Na^{125}I (corresponding to a volume of 5.0 μL) and 1.0 g/cm^3 water density, it was concluded that 5.0 μL of Na^{125}I corresponded to a concentration of 0.33 μM in the present study. Therefore, two ratios were chosen during radionuclide labeling based on parameter concentration and optimization. The HN-to-Na^{125}I ratios were set to 1:1 and 5:1. The labeling efficiency was represented via radioactive activity percentage of ^{125}I-HN from the total of Na^{125}I (calculated using the formula provided in section 2.6). Tyrosine is a recognized radionuclide labeling linker that was used as a positive control. Table 3 indicates that 1.06 mCi ^{125}I-HN was collected with a labeling efficiency of 82.8% at a molar ratio of 1:1, which was higher than 65.6% for 0.84 mCi ^{125}I-Tyr. The labeling efficiency of ^{125}I (85.7%) was not significantly elevated with the increase in HN concentration. To further verify the reliability of radionuclide ^{125}I labeling efficiency of HN and avoid radionuclide overuse, additional data were further obtained from three independent experiments in the low levels of radionuclide ^{125}I. The results in Table S1 showed that ^{125}I-HN had a similar labeling efficiency to that in Table 3. These results suggested that ^{125}I was close to being utilized completely with a minimal or justified losses at the two ratios described.

Table 1 Optimization of HN Labeling Parameters

Ratio	HN (μM)	Na^{127}I (μM)	Peak area-269 (10^6)	Peak area-395 (10^6)	Peak area-521 (10^6)	Labeling Efficiency (%)
1:0	0.33	0	68.9 ± 0.2	0	0	0
0.5:1	0.165	0.33	0	0	29.2 ± 0.5	100
1:1	0.33	0.33	5.3 ± 0.4	11.8 ± 0.8	43.7 ± 1.2	91.3 ± 0.6
3:1	0.825	0.33	108.6 ± 10.5	62.8 ± 6.5	37.9 ± 0.9	48.1 ± 4.2
5:1	1.65	0.33	257 ± 32.4	89.0 ± 4.1	19.8 ± 0.7	30.0 ± 3.5
10:1	3.3	0.33	551 ± 42.6	84.0 ± 5.2	18.9 ± 0.6	15.8 ± 1.6

Table 2 Labeling Efficiency of HN Obtained by ICP-OES Method

Ratio	HN (μM)	$Na^{127}I$ (μM)	^{127}I-HN (μM)	Labeling efficiency (%)
1:1	0.33	0.33	0.30 ± 0.04	92.4 ± 11.1
5:1	1.65	0.33	0.31 ± 0.04	94.3 ± 13.4

Table 3 Labeling Efficiency of ^{125}I for HN

Compounds	$Na^{125}I$ (mCi)	^{125}I-HN / ^{125}I-Tyr (mCi)	Labeling efficiency (%)
HN (0.33 μM)	1.28	1.06	82.8
HN (1.65 μM)	1.28	1.08	85.7
Tyr (0.33 μM)	1.28	0.84	65.6
Tyr (1.65 μM)	1.28	0.89	69.5

Preparation and Characterization of Nanocarriers

Eight representative NCs with different compositions, shapes, sizes, and surface charges were prepared and collected to verify that ^{125}I-HN can be used to combine various NCs. These included metal oxide NCs (CeO_2, La_2O_3), non-metallic NCs (mesoporous SiO_2, graphene oxide GO, and carbon nanotubes COOH-CNTs), and polymer NCs (different long cellulose nanofibers CNF-1, CNF-2; polyethyleneimine-functionalized cellulose nanofibers with different surface charges PEI-CNF-1).

The physicochemical properties of these NCs were characterized using TEM, AFM, zeta potential, and dynamic light scattering analyzer. TEM images (Figure 5A) showed that CeO_2 NCs were rod shaped with a length of 100–200 nm. La_2O_3 NCs exhibited sphere shapes with a diameter of 50–150 nm. SiO_2 NCs displayed uniform spherical morphologies

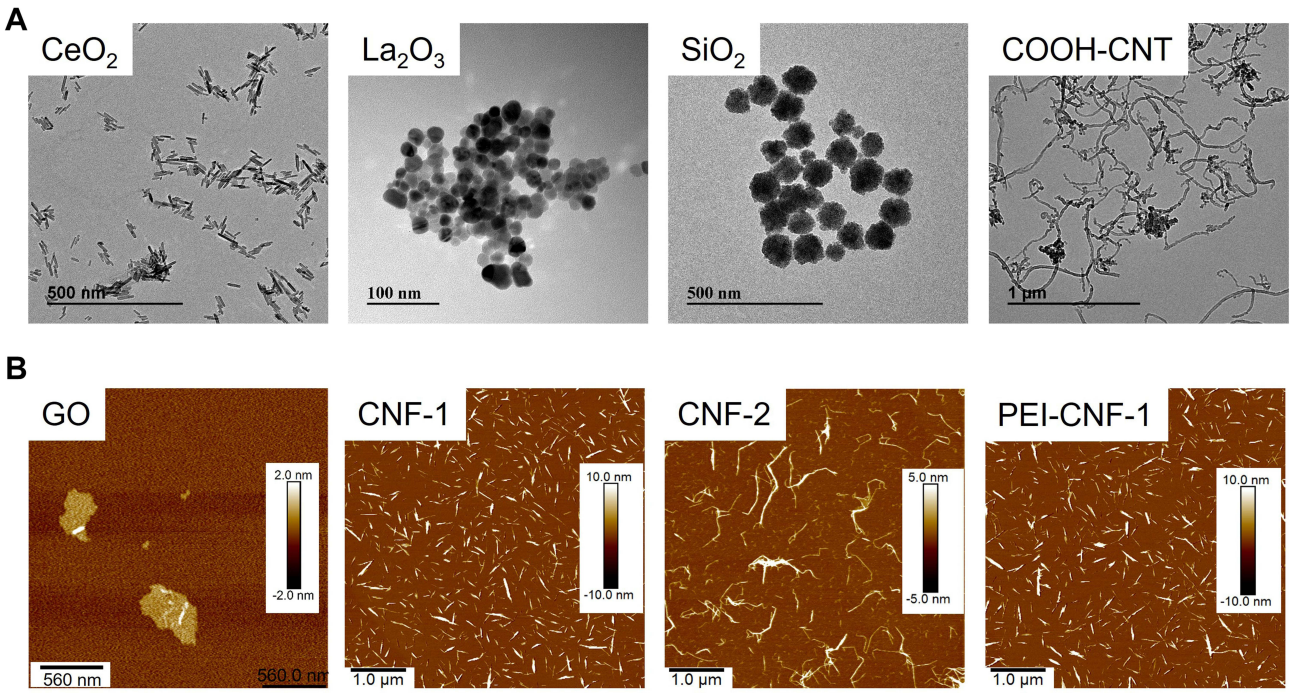

Figure 5 The Electron Microscopy for NC Morphologies. (**A**) TEM and (**B**) AFM images of NCs. A drop of NC suspension (50 μg/mL) was placed on a grid or mica plate and then dried at room temperature for TEM or AFM observations.

with mesoporous holes (Figure 5A). COOH-CNTs had fiber shapes with lengths of 500–700 nm (Figure 5A). AFM was used to visualize the morphologies of GO, CNFs, and PEI-CNF-1 due to the low electron density. GO sheet thickness from the edge was measured to be ~1.0 nm, while CNF-1 and CNF-2 had fiber morphologies with different lengths but similar diameters of −10.0 ~ 10.0 nm (Figure 5B). CNF-1 showed 600 ~ 700 nm lengths, while CNF-2 had longer lengths of 1300 ~ 1400 nm. In addition, CNF-1 and PEI-CNF-1 had the same length and diameter morphologies. NC surface charges and hydrodynamic sizes or lengths were determined in deionized water (DI H_2O) (Table 4). La_2O_3, CeO_2, and PEI-CNF-1 demonstrated positive surface charges with zeta potentials of +10 to +30 mV. CNFs, SiO_2, GO, and COOH-CNTs had negative charges (−30 to −10 mV). Compared to their pristine sizes or lengths shown in Figure 5, all these particles showed some agglomeration in DI H_2O.

Synthesis and in vivo Imaging of ^{125}I-NCs

^{125}I-HN was utilized to label the NCs with various properties to visualize their in vivo interaction, with the organism using radiological imaging. For the NCs with multiple functional groups (hydroxyl, carboxyl, or amino groups) on their surface, such as GO, COOH-CNT, CNFs, and PEI-CNF-1, the NCs were combined with ^{125}I-HN using the EDC/NHS method to complete ^{125}I labeling. The NCs without functional groups, such as CeO_2, La_2O_3, and SiO_2, were first functionalized with APTES to add amino groups onto the surface. To detect the functional groups on the surface of NCs, FT-IR NC spectra from 4000 to 500 cm^{-1} were obtained. As shown in Figure S1, pristine NCs (GO, COOH-CNT, CNFs, and PEI-CNF-1) or NCs functionalized with APTES (CeO_2, La_2O_3, and SiO_2) showed the characteristic absorption peaks at ~1,710 cm^{-1}, reflecting the stretching vibration of the carbonyl group (–C=O) or at ~3,444 cm^{-1}, reflecting the –NH bending vibration. The results indicated that these NCs had the essential condition for surface modification of ^{125}I-HN using the EDC/NHS method.

Then, ^{125}I labeling was implemented using the same method as described above. Despite the difference in labeling efficiency (33.0 ~ 85.8), the radioactivity value of all ^{125}I-NCs exceeded 0.05 mCi/100 μL (Table 5). Some ^{125}I-NC values were >0.10 mCi/100 μL. The radioactivity value of all ^{125}I-NCs met the necessary conditions for observing their distribution using in vivo SPECT/CT imaging (sensitivity >13,000 cps/MBq) in the present study. Similar to Tables 3 and S1, additional data were obtained from three independent experiments in the low levels of radionuclide ^{125}I to further verify the reliability of radionuclide ^{125}I labeling efficiency of NCs. The results in Table S2 showed that ^{125}I-NCs had a similar labeling efficiency to that in Table 5. To examine the stability of ^{125}I-NCs under the physiological conditions, the radioactivity change in ^{125}I-NCs was investigated before and after phosphate-buffered saline (0.9% NaCl) treatment for 5 days. Having ruled out the decay of radionuclide ^{125}I itself, the radioactive stability of ^{125}I-NCs was obtained by calculating the ratio of radioactive activity at two time points (days 1 and 5). The results in Figure S2 showed that the radioactive stability of all ^{125}I-NCs was maintained above 90%, indicating that the decomposition efficiency of ^{125}I-NCs was low.

Table 4 NC Size and Zeta-Potential

NCs	Diameter or Length (nm)	Zeta-Potential (mV)
CeO_2	148 ± 4	10.6 ± 2.6
La_2O_3	107 ± 7	30.1 ± 1.1
SiO_2	42 ± 5	−17.4 ± 0.6
GO	584 ± 30	−21.6 ± 0.5
COOH-CNT	620 ± 69	−26.3 ± 2.1
CNF-1	702 ± 59	−13.5 ± 1.7
CNF-2	1368 ± 104	−12.4 ± 1.8
PEI-CNF-1	632 ± 10	22.2 ± 1.6

Table 5 Radioactivity Value of ^{125}I-HN Labeling for NCs

NPs	CeO_2	La_2O_3	SiO_2	GO	COOH-CNT	CNF-1	CNF-2	PEI-CNF-1
^{125}I-HN (mCi)	1.06	1.06	1.06	1.06	1.06	1.06	1.06	1.06
^{125}I-NCs (mCi)	0.91	0.44	0.63	0.73	0.58	0.47	0.49	0.35
Labeling efficiency (%)	85.8	41.5	59.4	68.8	54.7	44.3	46.2	33.0
^{125}I-NCs (mCi/100 μL)	0.18	0.08	0.12	0.14	0.11	0.09	0.09	0.07

To observe the behavior of ^{125}I-NCs, excluding CNF-2 and PEI-CNF-1, at different nano–bio interfaces (enterocoelia, lung, and blood vessels), their distribution was visualized in vivo using SPECT/CT on days 1 and 5 after intraperitoneal injection, intratracheal instillation, and intravenous injection. All obtained images were of high resolution (Figures 6A–C). Radionuclides delivered via intraperitoneal injection in mice were mainly concentrated in the abdominal cavity. Radionuclides delivered via intratracheal instillation were mainly concentrated in the lung. Interestingly, for all ^{125}I-NCs except SiO_2 and CeO_2, radionuclides delivered via intravenous injection were observed in the liver and lung, and radioactive activity was present only in the liver for SiO_2 and CeO_2. In addition, ^{125}I-NC retention was also observed. All ^{125}I-NCs showed time-dependent clearance via different routes of administration over the course of 5 days. For quantification of ^{125}I-NCs in tissues, animal organ tissue samples were collected after a 5-day exposure (Figures 6D–F). For intraperitoneal injection, almost all ^{125}I-NCs showed the highest relative radioactivity (the percentage of current activity used as total activity) in the intestine, followed by the colon. For intratracheal instillation, all ^{125}I-NCs showed the highest relative radioactivity in the lung, followed by the colon. For intravenous injection, ^{125}I-NCs showed the highest relative radioactivity in the lung, followed by the heart, kidney, and liver. It is worth noting that the

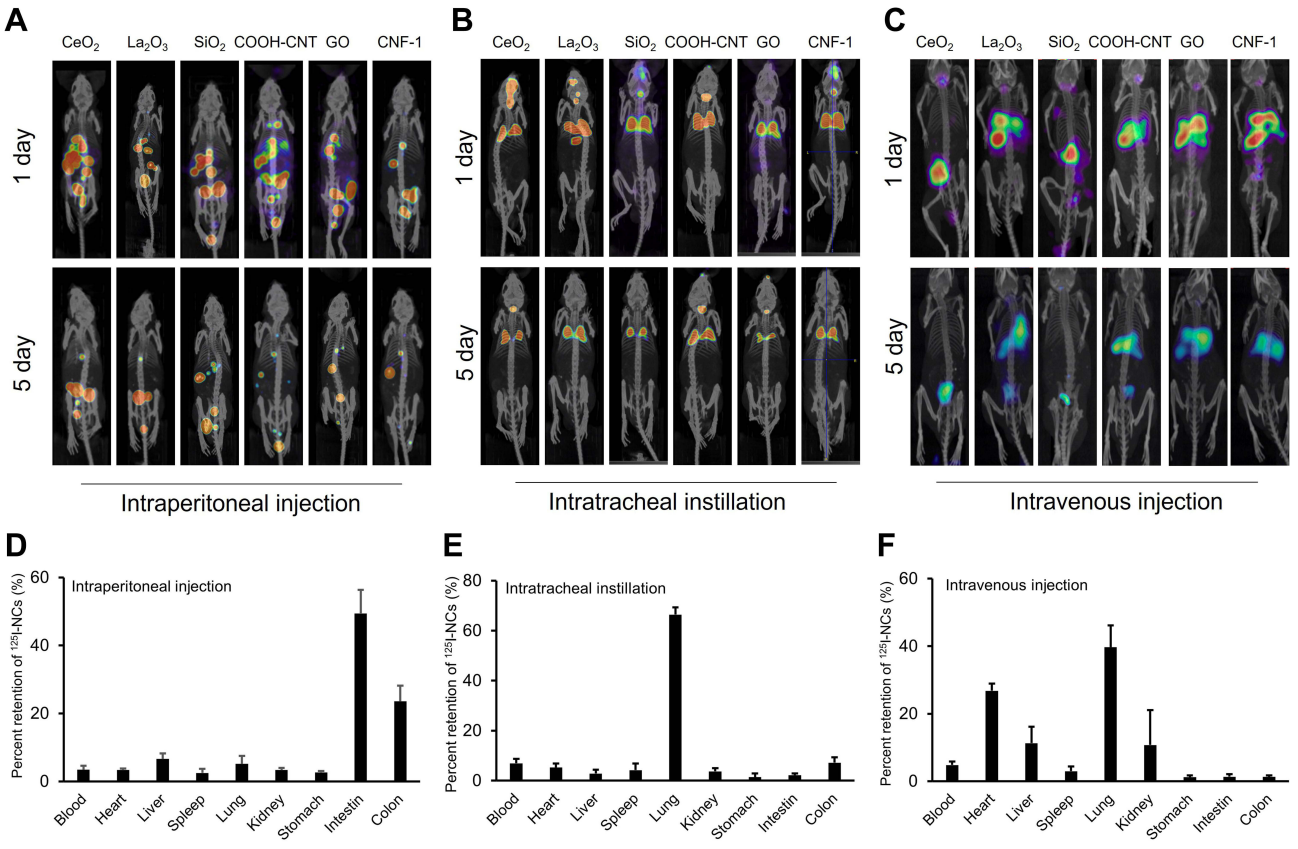

Figure 6 SPECT/CT Images of ^{125}I-NCs in Different Nano–Bio Interfaces in Mice. (**A**)–(**C**) Distribution and retention of ^{125}I-NCs in mice were visualized using SPECT/CT imaging after different administration of ^{125}I-NCs 1 and 5 days post-injection; (**D**)–(**F**) Tissue distribution of ^{125}I-NCs determined using radioactivity assay.

https://doi.org/10.2147/IJN.S446564 DovePress

radioactivity value in the same tissues of different ^{125}I-NCs was integrated in the final quantitative experiment to track their main flow direction in vivo.

Discussion

It is important to investigate the distribution of NCs, which is related to metabolism and clearance. Considering the biomedical applications of NCs in NMR imaging in vivo, the present study focused on radionuclide labeling of NCs and their imaging using SPECT/CT.

Previous studies revealed that the NCs needed to be first modified by Tyr, PEI, or polyethylene glycol (PEG) if NC radiolabeling was desired.[34,35] Fox example, a cancer catalytic internal radiotherapy study by Su et al used Auger electrons for an in-situ tumor to construct active sites in a TiO_2 nanocatalyst, which was labeled by radionuclide ^{125}I after the Tyr modification on its surface.[36] Similarly, Qin et al reported a nucleus-targeted internal conversion electron-based cancer therapy strategy induced by nanomicelles, which was labeled by radionuclide ^{125}I after the PEG modification on its surface.[37] Thus, it is evident that the radionuclide ^{125}I labeling method for NCs employing corresponding ligand design cannot be replicated and applied on a large scale. Therefore, it is necessary to establish a more universal radiolabeling method for NCs. For this purpose, a novel small molecule HN compound that can bind radionuclide ^{125}I with high efficiency was synthesized based on the substitution reaction. It had the following advantages compared to the traditional radionuclide labeling linker: i) good solubility, which canceled the solubility limitation of Tyr affected by its isoelectric point and reduced the requirement for reaction conditions; ii) more comprehensive adaptability. Radionuclide ^{125}I labeling can be performed on eight kinds of NCs with different physicochemical properties, including metal oxides, carbon nanomaterials, and nanofibers; iii) higher labeling efficiency. Compared to conventional Tyr linker, the labeling efficiency of radionuclide ^{125}I increased from about 50% to 80%. Therefore, HN shows a very good potential for the labeling capacity of radionuclide ^{125}I.

Despite the detailed and elaborate investigation of ^{125}I labeling and in vivo distribution and retention of NCs, there were three important limitations in the present study that need to be addressed in future research. First, only one radionuclide type was selected for testing. Different radionuclides, such as ^{125}I, ^{131}I, and ^{99}Tm, have a number of applications in nuclear medicine.[38] ^{125}I is used to kill tumors and trace the distribution and metabolism of NCs in vivo. ^{131}I is used to target and kill tumors, while ^{99}Tm is used to observe NC dynamics in blood circulation in a short period of time. However, only ^{125}I was explored in the present study. Compound HN was only used for ^{125}I labeling and was not validated in its role of binding to other radionuclides. Therefore, a single radionuclide labeling study may limit its widespread use. Second, NC imaging was performed after intraperitoneal injection and intratracheal instillation. Studies on oral administration and intravenous injection of NCs were not performed. However, considering that the focus of the present study was to only investigate the NC radionuclide labeling efficiency, the in vivo NC distribution was observed using SPECT/CT imaging after radionuclide NC labeling regardless of administration route. Oral administration and intravenous injection will be addressed in future studies. Finally, NCs generally exhibit targeting properties, but the NCs screened in the present study did not have the characteristics necessary to target tumors or other diseases. In addition, studying whether NCs have targeting properties using SPECT/CT imaging might prove particularly meaningful. Therefore, radionuclide labeling and imaging of NCs with targeting properties should be the focus of the follow-up studies.

Conclusion

In the present study, a novel small molecule compound HN was designed and synthesized as a linker. This compound has two functions: to bind NCs and to bind ^{125}I. Subsequently, it was observed that HN can efficiently label radionuclide ^{125}I using optimal reaction conditions for HN binding of iodine. Further observation showed that ^{125}I-HN can also label NCs with different physicochemical properties and demonstrated efficient labeling efficiency. In view of the lack of broad-spectrum radiolabeled NCs for long-term observation of their biological distribution and effects, SPECT/CT imaging technology was used to analyze the biological distribution and metabolism of ^{125}I-NCs under different exposure pathways (intraperitoneal injection, intratracheal instillation, and intravenous injection). The results suggested that ^{125}I-NCs play an important role in different research fields, such as NC tumor therapy and immune and inflammatory response.

Ethics Approval and Informed Consent

Animal experiments were approved by the Animal Research Committee at SOOCHOW. All animals were operated in accordance with the Guidelines for The Care and Use of Experimental Animals of Soochow University.

Acknowledgments

This work was supported by the Special Project of Suzhou Clinical Key Disease's Diagnosis and Treatment (LCZX202208), Case Cohort Project from Gusu School, Nanjing Medical University (GSKY20220408), Jiangsu Provincial Maternal and Child Health Scientific Project (F202044), and Suzhou "Rejuvenating Health through Science and Education" Youth Science Project (KJXW2021032). The authors would like to thank Professor Meilin Wang from the School of Public Health, Nanjing Medical University, China, for comments and suggestions to manuscript preparation, as well as State Key Laboratory of Radiation Medicine and Protection, Soochow University, China, for providing equipment to conduct the experiment.

Author Contributions

All authors made a significant contribution to the work reported, whether that is in the conception, study design, execution, acquisition of data, analysis and interpretation, or in all these areas; took part in drafting, revising or critically reviewing the article; gave final approval of the version to be published; have agreed on the journal to which the article has been submitted; and agree to be accountable for all aspects of the work.

Disclosure

The authors declare no conflict of interest.

References

1. Saito Y, Nose N, Iida T, et al. In vivo tracking transplanted cardiomyocytes derived from human induced pluripotent stem cells using nuclear medicine imaging. *Front Cardiovasc Med*. 2023;10:1261330. doi:10.3389/fcvm.2023.1261330
2. Kroeger EA, Rupp A, Gregor J. Misuse of a medical radioisotope: ^{125}i labeled playing cards in Germany, a case study. *Health Phys*. 2020;119(1):128–132. doi:10.1097/HP.0000000000001245
3. Zhou X, Zhang W, Dou M, et al. ^{125}I seeds inhibit proliferation and promote apoptosis in cholangiocarcinoma cells by regulating the AGR2-mediated p38 MAPK pathway. *Cancer Lett*. 2022;524:29–41. doi:10.1016/j.canlet.2021.10.014
4. E J-GI, Sabater S, Martinez-Gutierrez R, et al. LDR brachytherapy offers superior tumor control to single-fraction HDR prostate brachytherapy: a prospective study. *Prostate*. 2023;83(11):1068–1075. doi:10.1002/pros.24548
5. Yang M, You Y, Wang X, et al. I-125 seeds brachytherapy combined with immunotherapy for MET amplification in non-small cell lung cancer from clinical application to related lncRNA mechanism explore: a case report. *Front Cell Dev Biol*. 2023;11:1176083. doi:10.3389/fcell.2023.1176083
6. Huang S, Wu Y, Li C, et al. Tailoring morphologies of mesoporous polydopamine nanoparticles to deliver high-loading radioiodine for anaplastic thyroid carcinoma imaging and therapy. *Nanoscale*. 2021;13(35):15021–15030. doi:10.1039/D1NR02892H
7. K SS, Kumar Y, T PK, et al. Development of a ^{125}I source for its application in bone densitometry. *Appl Radiat Isot*. 2012;70(3):470–477. doi:10.1016/j.apradiso.2011.11.010
8. Wu Y, Yao Y, Zhang J, et al. Tumor-targeted injectable double-network hydrogel for prevention of breast cancer recurrence and wound infection via synergistic photothermal and brachytherapy. *Adv Sci*. 2022;9(24):e2200681. doi:10.1002/advs.202200681
9. Nosrati Z, Pl E, Rodríguez-Rodr Í, et al. Simultaneous SPECT imaging with ^{123}I and ^{125}I-a practical approach to assessing a drug and its carrier at the same time with dual imaging. *Int J Pharm*. 2021;606:120884. doi:10.1016/j.ijpharm.2021.120884
10. Huang H, Zhu H, Xie Q, et al. Evaluation of ^{124}I-JS001 for hPD1 immuno-PET imaging using sarcoma cell homografts in humanized mice. *Acta Pharm Sin B*. 2020;10(7):1321–1330. doi:10.1016/j.apsb.2020.02.004
11. Liu R, Shi J, Ge X, et al. Similar therapeutic effects of ^{125}I seed radiotherapy and γ-ray radiotherapy on lacrimal gland adenoid cystic carcinoma. *Int J Ophthalmol*. 2021;14(4):547–553. doi:10.18240/ijo.2021.04.11
12. Chen L, Ge J, Huang B, et al. Anchoring group mediated radiolabeling for achieving robust nanoimaging probes. *Small*. 2021;17(51):e2104977. doi:10.1002/smll.202104977
13. Zhong J, Zhang Q, Zhang Z, et al. Albumin mediated reactive oxygen species scavenging and targeted delivery of methotrexate for rheumatoid arthritis therapy. *Nano Res*. 2022;15(1):153–161. doi:10.1007/s12274-021-3449-1
14. Wang D, Yue J, Cao Q, et al. ICG-loaded and 25 I-labeled theranostic nanosystem for multimodality imaging-navigated phototherapy of breast cancer. *Biomater Sci*. 2022;11(1):248–262. doi:10.1039/D2BM01551J
15. Kondo Y, Kimura H, Sasaki M, et al. Effect of water on direct radioiodination of small molecules/peptides using copper-mediated iododeboronation in water-alcohol solvent. *Acs Omega*. 2023;8(27):24418–24425. doi:10.1021/acsomega.3c01974
16. Sun J, Huangfu Z, Yang J, et al. Imaging-guided targeted radionuclide tumor therapy: from concept to clinical translation. *Adv Drug Deliv Rev*. 2022;190:114538. doi:10.1016/j.addr.2022.114538

17. Yi X, Xu M, Zhou H, et al. Ultrasmall hyperbranched semiconducting polymer nanoparticles with different radioisotopes labeling for cancer theranostics. *Acs Nano*. 2018;12(9):9142–9151. doi:10.1021/acsnano.8b03514
18. Gu X, Wei Y, Fan Q, et al. cRGD-decorated biodegradable polytyrosine nanoparticles for robust encapsulation and targeted delivery of doxorubicin to colorectal cancer in vivo. *J Control Release*. 2019;301:110–118. doi:10.1016/j.jconrel.2019.03.005
19. Bouhlel Z, A AA, E WD, et al. Labelling strategy and membrane characterization of marine bacteria Vibrio splendidus by in vivo ^{2}H NMR. *Biochim Biophys Acta Bio*. 2019;1861(4):871–878. doi:10.1016/j.bbamem.2019.01.018
20. Card M, Alejandro R, Roxbury D. Decoupling individual optical nanosensor responses using a spin- coated hydrogel platform. *ACS Appl Mater Interfaces*. 2022;15(1):1772–1783. doi:10.1021/acsami.2c16596
21. Liu R, Yao T, Liu Y, et al. Temperature-sensitive polymeric nanogels encapsulating with β-cyclodextrin and ICG complex for high- resolution deep-tissue ultrasound-switchable fluorescence imaging. *Nano Res*. 2020;13(4):1100–1110. doi:10.1007/s12274-020-2752-6
22. J GP, Man F, J BP, et al. Direct cell radiolabeling for in vivo cell tracking with PET and SPECT Imaging. *Chem Rev*. 2022;122(11):10266–10318. doi:10.1021/acs.chemrev.1c00767
23. Kostiv U, Lobaz V, Kucka J, et al. A simple neridronate-based surface coating strategy for upconversion nanoparticles: highly colloidally stable ^{125}I-radiolabeled NaYF 4: Yb^{3+}/Er^{3+}@PEG nanoparticles for multimodal in vivo tissue imaging. *Nanoscale*. 2017;9(43):16680–16688. doi:10.1039/C7NR05456D
24. L BKC, J AW, Sudlow G, et al. Dual-radiolabeled nanoparticle SPECT probes for bioimaging. *Nanoscale*. 2015;7(2):440–444. doi:10.1039/C4NR05269B
25. S FN, A E-SH, M A-MA, et al. Comparative study on radiolabeling and biodistribution of core-shell silver / polymeric nanoparticles-based theranostics for tumor targeting. *Int J Pharm*. 2017;529(1–2):123–133. doi:10.1016/j.ijpharm.2017.06.044
26. Enrique M, Mariana O, F MS, et al. Multifunctional radiolabeled nanoparticles: strategies and novel classification of radiopharmaceuticals for cancer treatment. *J Drug Target*. 2015;23(3):191–201. doi:10.3109/1061186X.2014.988216
27. Pant K, Sedlacek O, A NR, et al. Radiolabelled polymeric materials for imaging and treatment of cancer: quo vadis? *Adv Healthc Mater*. 2017;6(6):1601115. doi:10.1002/adhm.201601115
28. Yang L, Zhang C, Liu J, et al. ICG-Conjugated and ^{125}I-labeled polymeric micelles with high biosafety for multimodality imaging-guided photothermal therapy of tumors. *Adv Healthc Mater*. 2020;9(5):e1901616. doi:10.1002/adhm.201901616
29. Prasad KN, Cole WC, Haase GM. Radiation protection in humans: extending the concept of as low as reasonably achievable (ALARA) from dose to biological damage. *Br J Radiol*. 2004;77(914):97–99. doi:10.1259/bjr/88081058
30. Ferro-Flores G, E O-GB, L S-C-C, et al. Multifunctional radiolabeled nanoparticles for targeted therapy. *Curr Med Chem*. 2014;21(1):124–138. doi:10.2174/09298673113209990218
31. Chen L, Zhong X, Yi X, et al. Radionuclide ^{131}I labeled reduced graphene oxide for nuclear imaging guided combined radio- and photothermal therapy of cancer. *Biomaterials*. 2015;66:21–28. doi:10.1016/j.biomaterials.2015.06.043
32. Ma R, Zheng H, Liu Q, et al. Exploring the interactions between engineered nanomaterials and immune cells at 3D nano-bio interfaces to discover potent nano-adjuvants. *Nanomedicine*. 2019;21:102037. doi:10.1016/j.nano.2019.102037
33. Sadeghzadeh M, J DF, Sheibani S, et al. Radioiodination of 4-benzyl-1-(3-iodobenzylsulfonyl)piperidine, 4-(3-iodobenzyl)-1-(benzylsulfonyl)piperazine and their derivatives via isotopic and non-isotopic exchange reactions. *J Radioanal Nucl Chem*. 2014;302(3):1119–1125. doi:10.1007/s10967-014-3347-z
34. Ge J, Zhang Q, Zeng J, et al. Radiolabeling nanomaterials for multimodality imaging: new insights into nuclear medicine and cancer diagnosis. *Biomaterials*. 2020;228:119953. doi:10.1016/j.biomaterials.2019.119553
35. Pei P, Liu T, Shen W, et al. Biomaterial-mediated internal radioisotope therapy. *Mater Horiz*. 2021;8(5):1348–1366. doi:10.1039/D0MH01761B
36. Su W, Wang H, Wang T, et al. Auger electrons constructed active sites on nanocatalysts for catalytic internal radiotherapy. *Adv Sci*. 2020;7(10):1903585. doi:10.1002/advs.201903585
37. Qin Y, Shen M, Liu X, et al. Correction to "photo-driven delivery of ^{125} i-labeled nanomicelles for nucleus-targeted internal conversion electron-based cancer therapy". *Acs Appl Mater Interfaces*. 2022;14(42):48323–48325. doi:10.1021/acsami.1c13249
38. Michotte C. Radionuclide activities. *Nat Phys*. 2023;19(8):1220. doi:10.1038/s41567-023-02166-5